

HEOM-Based Numerical Framework for Quantum Simulation of Two-Dimensional Vibrational Spectra in Molecular Liquids (HEOM-2DVS)

Ryotaro Hoshino[✉] and Yoshitaka Tanimura^{✉,a)}

Department of Chemistry, Graduate School of Science, Kyoto University, Kyoto 606-8502, Japan

(Dated: Last updated: 29 January 2026)

The multi-mode anharmonic Brownian motion model offers a universal framework for simulating molecular vibrations in condensed phases. When vibrational energy surpasses thermal excitation, quantum effects become significant, necessitating a rigorous treatment of system–bath entanglement. The hierarchical equations of motion (HEOM) provide a powerful methodology for simulating such open quantum systems. In this context, two-dimensional vibrational spectroscopy (2DVS) constitutes a powerful probe for elucidating the complex dynamics of molecular processes, both experimentally and theoretically. This work introduces a computational implementation, HEOM-2DVS, for treating non-Markovian open quantum dynamics that encompass energy relaxation, dephasing, thermal excitation, and related processes arising from non-perturbative and nonlinear interactions between selected vibrational modes and their thermal environments. To validate the theoretical framework, we computed two-dimensional correlation infrared spectra for three coupled intramolecular vibrational modes of water. The results clarify how intermolecular interactions and mode–bath couplings manifest as characteristic changes in the spectral features of 2DVS. The HEOM-2DVS program, written in C++, is provided as supporting material.

I. INTRODUCTION

The vibrational dynamics of molecules in condensed phases have increasingly been recognized as crucial factors shaping chemical reactivity. In particular, intramolecular motions in solution—most prominently the OH stretching vibration of water—have garnered significant interest as active contributors to reactivity.^{1,2} Rather than serving as a passive thermal background, molecular environments exhibit ultrafast phenomena, including energy and phase relaxation. In hydrogen-bonding solvents, these dynamics may further involve hydrogen-bond rearrangement and proton migration, all of which complicate its analysis.^{3–6}

To elucidate these dynamics, femtosecond-resolved measurements are indispensable, as they coincide with the intrinsic timescales of fundamental chemical processes, including bond rearrangements and chemical reactions. Two-dimensional vibrational spectroscopy (2DVS) has established itself as a powerful tool for resolving vibrational mode correlations, coherence lifetimes, and pathways of energy flow with exceptional spectral precision.^{7–13} Its acute sensitivity to anharmonicity, mode coupling, and vibrational coherence allows rigorous quantification of the relaxation–dephasing mechanisms that govern spectral broadening.^{14–19} Since these nonlinear spectral signatures are intimately tied to quantum dissipative dynamics—phenomena beyond the current reach of molecular dynamics (MD) simulations—robust theoretical modeling remains indispensable for their interpretation and full exploitation.²⁰

For decades, MD simulations have served as a principal framework for investigating the dynamical properties of solutions.^{21–35} Classical MD, however, is intrinsically incapable of incorporating essential quantum mechanical phenomena—zero-point energy, tunneling, and quantum thermal fluctuations—that are indispensable for a faithful description of vibrational dephasing and couplings among intermolecular modes. Quantum MD methodologies, such as path-integral Centroid MD (PI-CMD), have been advanced to address these deficiencies; yet their application to 2DVS remains computationally formidable.^{36–38} To confront these challenges, MD-based modeling frameworks have been advanced, incorporating stochastic dynamics³⁹ and excitonic wavefunction approaches.⁴⁰ Machine-learning (ML) methodologies leveraging MD trajectories have likewise been developed.^{41–43}

For accurate modeling of vibrational dephasing and relaxation, nonlinear, non-perturbative, and non-Markovian system-bath (S–B) interactions must be incorporated, since the vibrational echo signal originates from S–B entanglement.^{44,45} Our group has performed multidimensional spectral analyses using the multimode anharmonic Brownian (MAB) model,^{20,46} and developed Hierarchical Fokker–Planck equations (HFPE) in both classical (CHFPE)^{47–50} and quantum (DHEOM-MLWS) forms.^{51,52} These enable numerically precise simulations of nonlinear spectra in complex systems. By calibrating CHFPE to reproduce classical MD benchmarks^{43,48} and applying QHFPE for quantum-level insights,^{51,52} the quantum nature of vibrational dynamics is revealed. In contrast, classical simulations remain suitable for 2DVS—such as 2D Raman^{21–23} and 2D THz-Raman spectroscopy^{31–33,47,50}—where thermal excitation suppresses quantum coherence.

For intramolecular modes exhibiting significant quan-

^{a)}Author to whom correspondence should be addressed: tanimura.yoshitaka.5w@kyoto-u.jp

tum effects, computational approaches to 2DVS have thus far been developed within the QHFPE framework for two-mode MAB models, typically involving stretching and bending vibrations.^{51,52} While such models capture mode-mode coupling, a three-mode formulation is required to describe energy transfer pathways and coherence dynamics. Given the experimental precision of 2DVS in resolving these processes, extending to three-mode models is indispensable. We previously carried out classical simulations of an MAB system, incorporating the symmetric, antisymmetric, and bending vibrational modes^{49,50}—but these results highlight the limitations of classical treatments in fully accounting for ultrafast coherence-driven relaxation.⁴⁶ Therefore, in this work, we present an HEOM-based computational framework for simulating 2D correlation IR spectra^{8–10,53–58} extending previous approaches to treat three interacting intramolecular modes within an open quantum dynamics setting.^{49–52} The resulting implementation, HEOM-2DVS, enables non-Markovian simulations that capture energy relaxation, dephasing, thermal excitation, and related effects arising from non-perturbative and nonlinear mode-bath interactions.

This paper is organized as follows. Section II introduces the MAB model and the HEOM for intramolecular vibrational modes. Section III briefly describes the structure of our codes, and Section IV demonstrates their capability through simulations of linear absorption spectra and 2D correlation IR spectra. Concluding remarks are provided in Section V.

II. MAB MODEL AND HEOM

A. MAB model

We consider a model consisting of three primary intramolecular modes. These modes are described by vibrational coordinates $\mathbf{q} = (q_1, q_2, q_3)$. Each mode is independently coupled to the other optically inactive modes, which constitute a bath system represented by an ensemble of harmonic oscillators. The total Hamiltonian can then be expressed as^{41–43,47–52}

$$\hat{H}_{tot} = \sum_s \left(\hat{H}_A^{(s)} + \hat{H}_I^{(s)} + \hat{H}_B^{(s)} + \hat{H}_C^{(s)} \right) + \sum_{s < s'} \hat{U}_{ss'}(\hat{q}_s, \hat{q}_{s'}), \quad (1)$$

where

$$\hat{H}_A^{(s)} = \frac{\hat{p}_s^2}{2m_s} + \hat{U}_s(\hat{q}_s) \quad (2)$$

is the Hamiltonian for the s th mode, with mass m_s , coordinate \hat{q}_s , and momentum \hat{p}_s ; and

$$\hat{U}_s(\hat{q}_s) = \frac{1}{2}m_s\omega_s^2\hat{q}_s^2 + \frac{1}{3!}g_{s^3}q_s^3 \quad (3)$$

is the anharmonic potential for the s th mode, described by the frequency ω_s and cubic anharmonicity g_{s^3} . The anharmonic coupling between the s th and s' th modes is given by

$$\hat{U}_{ss'}(\hat{q}_s, \hat{q}_{s'}) = g_{ss'}\hat{q}_s\hat{q}_{s'} + \frac{1}{6}(g_{s^2s'}\hat{q}_s^2\hat{q}_{s'} + g_{ss'^2}\hat{q}_s\hat{q}_{s'}^2), \quad (4)$$

where $g_{ss'}$ represents the second-order harmonicity, and $g_{s^2s'}$ and $g_{ss'^2}$ represent the third-order anharmonicity.

The bath Hamiltonian for the s th mode is expressed as^{44,59–62}

$$\hat{H}_B^{(s)} = \sum_{j_s} \left(\frac{\hat{p}_{j_s}^2}{2m_{j_s}} + \frac{m_{j_s}\omega_{j_s}^2\hat{x}_{j_s}^2}{2} \right), \quad (5)$$

where the momentum, coordinate, mass, and frequency of the j_s th bath oscillator are given by p_{j_s} , x_{j_s} , m_{j_s} and ω_{j_s} , respectively. The counter term, which maintains the translational symmetry of the system in the case $\hat{U}_s(\hat{q}_s) = \hat{U}_{ss'}(\hat{q}_s, \hat{q}_{s'}) = 0$ is defined as^{60,63}

$$\hat{H}_C^{(s)} = \Lambda^{(s)}\hat{V}_s^2(\hat{q}_s) \quad (6)$$

with the factor $\Lambda^{(s)} \equiv \sum_{j_s} \alpha_{j_s}^2/2m_{j_s}\omega_{j_s}^2$. The S-B interaction is expressed as

$$H_I^{(s)} = -V_s(\hat{q}_s) \sum_{j_s} \alpha_{j_s} \hat{x}_{j_s}, \quad (7)$$

where $V_s(q_s) \equiv V_{LL}^{(s)}q_s + V_{SL}^{(s)}q_s^2/2$ with the linear-linear (LL)^{59–62} and square-linear (SL) S-B interactions.^{63–65} The coupling strengths are expressed by $V_{LL}^{(s)}$, $V_{SL}^{(s)}$, and α_{j_s} . For a vibrational mode with weak anharmonicity, the LL interaction leads to energy relaxation, whereas the SL interaction results in vibrational dephasing.^{44,64}

We consider the optical measurements where the molecular system is interacting with a laser field, $E(t)$. The nonlinear elements of dipole are essential to 2D spectroscopy. Here we assume^{48–52}

$$\hat{\mu} = \sum_s \mu_s \hat{q}_s + \frac{1}{2!} \sum_{s,s'} \mu_{ss'} \hat{q}_s \hat{q}_{s'}, \quad (8)$$

where μ_s and $\mu_{ss'}$ are the linear and nonlinear elements of the dipole moment. For IR spectroscopies, the laser interaction is then expressed as $H_{IR}(t) = -E(t)\mu(\mathbf{q})$.

The system Hamiltonian can always be expressed in matrix form using the energy eigenstates of $\hat{H}_A^{(s)}$, denoted as $|n\rangle_s$ with eigenenergy $\hbar\omega_n^s = s \langle n | \hat{H}_A^{(s)} | n' \rangle_s$. Then for $\hat{H}_S \equiv \sum_s \hat{H}_A^{(s)} + \sum_{s < s'} \hat{U}_{ss'}(\hat{q}_s, \hat{q}_{s'})$ we have

$$\begin{aligned} \hat{H}_S = & \hbar \sum_s \sum_n \omega_n^s |n\rangle_s \langle n| \\ & + \hbar \sum_{s < s'} \sum_{n \neq n'} \Delta_{nn' mm'}^{ss'} |m\rangle_{s'} \langle n|_s \langle n'|_{s'} \langle m'|, \end{aligned} \quad (9)$$

where $\hbar\Delta_{nn' mm'}^{ss'} = s \langle n |_{s'} \langle m | \hat{U}_{ss'}(\hat{q}_s, \hat{q}_{s'}) | n' \rangle_s | m' \rangle_{s'}$.

The dipole moment is now expressed as

$$\hat{\mu} = \sum_s \sum_{n \geq n'} \mu_{nn'}^s |n\rangle_{ss} \langle n'| + \sum_{s < s'} \sum_{n_s \neq n'} \mu_{n,n'}^{s,s'} |n\rangle_{ss'} \langle n'|, \quad (10)$$

where $\mu_{nn'}^s = {}_s \langle n | \mu^s \hat{q}_s | n' \rangle_s$ and $\mu_{n,n'}^{s,s'} = {}_s \langle n | \hat{q}_s | n \rangle_{ss'} \langle n' | \hat{q}_{s'} | n' \rangle_{s'}/2$.

The total Hamiltonian is then given by

$$\hat{H}_{tot} = \hat{H}'_S - \sum_s \sum_{j_s} \alpha_{j_s} \hat{V}_s \hat{x}_{j_s} + \sum_s \sum_{j_s} \left[\frac{\hat{p}_{j_s}^2}{2m_{j_s}} + \frac{m_{j_s} \omega_{j_s}^2}{2} \hat{x}_{j_s}^2 \right], \quad (11)$$

where $\hat{H}'_S \equiv \hat{H}_S + \hat{H}_C$ and

$$\hat{H}_C = \hbar \sum_s \sum_{n \geq n'} \delta_{nn'}^s |n\rangle_{ss} \langle n'| \quad (12)$$

with

$$\hbar \delta_{nn'}^s = \Lambda^{(s)} {}_s \langle n | V_s^2(\hat{q}_s) | n' \rangle_s. \quad (13)$$

The system part of the S-B interaction is expressed as

$$\hat{V}_s = \sum_{n \geq n'} V_{nn'}^s |n\rangle_{ss} \langle n'|, \quad (14)$$

where $V_{nn'}^s \equiv {}_s \langle n | V_s(\hat{q}_s) | n' \rangle_s$.

The bath property is characterized by the spectral distribution function (SDF), defined as

$$J_s(\omega) \equiv \sum_{j_s} \frac{\alpha_{j_s}^2}{2m_{j_s} \omega_{j_s}} \delta(\omega - \omega_{j_s}). \quad (15)$$

The factor of the counter term is then expressed as

$$\Lambda^{(s)} = \int_0^\infty d\omega \frac{J_s(\omega)}{\omega}. \quad (16)$$

B. HEOM for MAB model

The noise operator associated with the s th intramolecular mode is defined by $\hat{X}_s \equiv \sum_{j_s} \alpha_{j_s} \hat{x}_{j_s}$. For a harmonic bath, noise correlations beyond third order vanish, and the dissipation can thus be fully characterized by the linear response function, $iL_1^{(s)}(t) = i\langle \hat{X}_s(t) \hat{X}_s - \hat{X}_s \hat{X}_s(t) \rangle_B / \hbar$, where $\hat{X}_s(t)$ is the Heisenberg representation of \hat{X}_s with respect to the bath Hamiltonian $\hat{H}_B^{(s)}$ (excluding the counter term), and $\langle \dots \rangle_B$ denotes the thermal average over the bath degrees of freedom. Correspondingly, thermal fluctuations are characterized by $L_2^{(s)}(t) = \langle \hat{X}_s(t) \hat{X}_s + \hat{X}_s \hat{X}_s(t) \rangle_B / 2$. The interplay between fluctuation and dissipation facilitates energy exchange, driving the system toward thermal equilibrium. This equilibrium condition is rigorously governed by

the quantum fluctuation-dissipation theorem.^{44,45,66} The combined kernel function, $L^{(s)}(t) = iL_1^{(s)}(t) + L_2^{(s)}(t)$, naturally emerges in the Feynman-Vernon influence functional formalism.⁶⁷

For the Drude SDF,

$$J_s(\omega) = \frac{m_s \zeta_s}{2\pi} \frac{\gamma_s^2 \omega}{\omega^2 + \gamma_s^2}, \quad (17)$$

they are evaluated as^{44,45}

$$iL_1^{(s)}(t) = -\frac{im_s \zeta_s \gamma_s^2}{2} e^{-\gamma_s t} \quad (18)$$

and

$$L_2^{(s)}(t) = \frac{m_s \zeta_s \gamma_s^2}{\beta \hbar} \sum_{k=1}^{K_s} \left[\frac{1}{\gamma_s} + \frac{2\eta_k \gamma_s}{\gamma_s^2 - \nu_k^2} \right] e^{-\gamma_s t} - \frac{m_s \zeta_s \gamma_s^2}{\beta \hbar} \sum_{k=1}^{K_s} \frac{2\eta_k \nu_k}{\gamma_s^2 - \nu_k^2} e^{-\nu_k t}, \quad (19)$$

where the parameters η_k^s and ν_k^s denote the Padé-approximated thermal coupling intensity and frequency.⁶⁸ The constant for the counter term is now given by

$$\Lambda^{(s)} = \frac{m_s \zeta_s \gamma_s}{2}. \quad (20)$$

For the MBA model [Eqs.(1)-(7)] with the Drude SDF [Eq. (17)], quantum hierarchical Fokker-Planck equations (QHFPE) have been formulated to describe two vibrational modes, encompassing both intramolecular and intermolecular dynamics.⁵¹ In parallel, classical hierarchical Fokker-Planck equations (CHFPE) have been developed to treat three vibrational modes.^{49,50} Hereafter, we refer to this as CHFPE-2DVS. Computational implementations of both approaches are publicly available.^{50,52}

Since this study focuses only on intramolecular vibrational modes, it is feasible to represent the reduced density operator using the eigenenergy states of each vibrational potential rather than phase-space coordinates. It is worth noting that, due to the classical nature induced by thermal baths, the phase-space representation remains advantageous for describing low-frequency intermolecular modes, offering lower computational cost.⁴⁷⁻⁵⁰

The HEOM obtained by transforming this phase-space representation into the energy-eigenvalue representation differs from the standard HEOM in that it requires explicitly including the counter term (12) as \hat{H}'_S in the system Hamiltonian.

We defined $\nu_0^s \equiv \gamma_s$, and introduce the Padé approximated frequencies ν_k^s for $k = \{1, 2, \dots, K_s\}$.⁶⁸ We also define the hyperoperators $\hat{A}^\times \hat{B} \equiv \hat{A} \hat{B} - \hat{B} \hat{A}$ and $\hat{A}^\circ \hat{B} \equiv \hat{A} \hat{B} + \hat{B} \hat{A}$, for arbitrary operators \hat{A} and \hat{B} .

The HEOM for the Drude SDF is then expressed as⁴²

$$\begin{aligned} \frac{d}{dt} \hat{\rho}_{\{\mathbf{n}_s\}} = & - \left[\frac{i}{\hbar} \hat{H}_S^{\prime \times} + \sum_s \sum_{k=0}^{K_s} (n_k^s \nu_k^s) \right] \hat{\rho}_{\{\mathbf{n}_s\}} \\ & - i \sum_s \sum_{k=0}^{K_s} n_k^s \hat{\Theta}_k^s \hat{\rho}_{\{\mathbf{n}_s - \mathbf{e}_s^k\}} \\ & - i \sum_s \sum_{k=0}^{K_s} \hat{V}_s^{\times} \hat{\rho}_{\{\mathbf{n}_s + \mathbf{e}_s^k\}}. \end{aligned} \quad (21)$$

The hierarchy elements are indexed by the set $\{\mathbf{n}_s\} \equiv (\mathbf{n}_1, \mathbf{n}_2, \mathbf{n}_3)$, where each \mathbf{n}_s is a multi-index defined as $\mathbf{n}_s = (n_0^s, n_1^s, \dots, n_{K_s}^s)$ for the three-mode case. All elements $\hat{\rho}_{\{\mathbf{n}_s\}}(t)$ with any negative index $n_k^s < 0$ are set to zero.

The notation $\{\mathbf{n}_s \pm \mathbf{e}_s^k\}$ indicates an increment or decrement of the k th component of \mathbf{n}_s , where \mathbf{e}_s^k is the unit vector corresponding to the k th frequency component in the s th bath. The operators are defined as follows:

$$\begin{aligned} \hat{\Theta}_0^{(s)} = & -i \frac{m_s \zeta_s \gamma_s^2}{2} \hat{V}_s^{\circ} \\ & + \frac{m_s \zeta_s \gamma_s}{\beta \hbar} \left(1 + \sum_{k=1}^{K_s} \frac{2 \eta_k^s \gamma_s^2}{\gamma_s^2 - \nu_k^{s2}} \right) \hat{V}_s^{\times}, \end{aligned} \quad (22)$$

and

$$\hat{\Theta}_{k>0}^{(s)} = -\frac{m_s \zeta_s \gamma_s^2}{\beta \hbar} \frac{2 \eta_k^s \nu_k}{\gamma_s^2 - \nu_k^2} \hat{V}_s^{\times}, \quad (23)$$

where the parameters η_k^s denotes the Padé-approximated thermal coupling.⁶⁸

C. Linear absorption and 2D correlation IR spectra

We now consider a model consisting of three primary intramolecular modes of the water molecule: (1) asymmetric stretch, (1') symmetric stretch, and (2) bending. These modes are described by dimensionless vibrational coordinates $\mathbf{q} = (q_1, q_1', q_2)$.⁴⁹

By representing intramolecular modes in terms of energy eigenstates, one can perform simulations and analyses based on optical Liouville pathways in electronically excited states.⁷ While calculating 2D correlation IR spectra within MD or Wigner representations requires additional effort to eliminate contributions from non-rephasing components,^{24,49,52} energy eigenstate representations allow a straightforward evaluation, as the calculation merely involves selecting the corresponding optical Liouville paths.^{53,54} However, because of nonlinear interactions between the molecule and the laser field, as well as among vibrational modes, a vast number of Liouville pathways must be considered for an accurate description. To illustrate this approach, we symbolically denote the

three-mode excited states as $|\mathbf{1}\rangle$ and $|\mathbf{2}\rangle$, as explained below.

We first note that the excitation frequencies of the intramolecular modes are much larger than thermal excitations. Therefore, the initial equilibrium state can be safely assumed to be the ground vibrational eigenstate of each mode, $|\mathbf{0}\rangle = |0_1, 0_1', 0_2\rangle$.

Let us denote the state resulting from applying the dipole operator $\hat{\mu}$ in Eq. (10) to this state once, symbolically, as $|\mathbf{1}\rangle$. The state $|\mathbf{1}\rangle$ contains components such as $\mu^{1'}|0_1, 1_1', 0_2\rangle$ and $\mu^{12}|1_1, 0_1', 1_2\rangle$, corresponding to single-excitation and double-excitation states. However, since the $\mu^{ss'}$ component is smaller than the μ^s component, the double excitation has only a minor effect.

After the time t_1 , a second application of the dipole operator to $|\mathbf{1}\rangle$ returns part of the components to the ground state as $\mu^{1'}|0_1, 0_1', 0_2\rangle$ or $\mu^{12}|0_1, 0_1', 0_2\rangle$. At the same time, it also generates higher-excitation contributions, collectively denoted as $|\mathbf{2}\rangle$, including $\mu^{1'}|0_1, 2_1', 0_2\rangle$, $\mu^{12}|2_1, 0_1', 0_2\rangle$, and $\mu^{1'2}|1_1, 1_1', 2_2\rangle$. During the time evolution t_1 , t_2 , and t_3 , excitation or relaxation may occur to various states other than $|\mathbf{1}\rangle$ due to mode-mode interactions characterized by the coupling strength $\Delta_{nn' mm'}^{ss'}$ and interactions with the bath. For short t_1 , however, such contributions are regarded as relatively minor.

1. Linear absorption (1D) spectra

In the density operator representation, the first-order response functions is expressed as^{44,45}

$$R^{(1)}(t_1) = \left(\frac{i}{\hbar} \right) \text{tr} \{ \hat{\mu} \mathcal{G}(t_1) \hat{\mu}^{\times} \hat{\rho}^{\text{eq}} \}, \quad (24)$$

where $\mathcal{G}(t)$ is the Green's function of the total Hamiltonian without a laser interaction, and $\hat{\rho}^{\text{eq}}$ is the equilibrium state. The Fourier transform of the above $I(\omega) = \int_0^\infty dt R^{(1)}(t) \exp(i\omega t)$ is equivalent to the linear absorption spectrum.

We evaluate Eqs. (24) in four steps.^{44,45}

- Set a factorized temporary initial condition at $t = -t_{\text{eq}}$ as $\hat{\rho}_{\{\mathbf{n}_s = \mathbf{0}\}}(-t_{\text{eq}}) = |\mathbf{0}\rangle\langle\mathbf{0}|$.
- Propagate the HEOM up to sufficiently long t_{eq} to attain the equilibrium state $\hat{\rho}_{\{\mathbf{n}_s\}}^{\text{eq}}$. If the vibrational excitation energy is sufficiently higher than the thermal excitation, the state remains equivalent to the temporal initial condition factorized with the bath.
- Excite the system at $t_1 = 0$ by $\hat{\rho}'(0) = \hat{\mu}^{\times} \hat{\rho}^{\text{eq}}$, which yields components in the states $|\mathbf{1}\rangle\langle\mathbf{0}|$ and $|\mathbf{0}\rangle\langle\mathbf{1}|$.
- Propagate the perturbed hierarchy under the HEOM, Eqs. (21)–(23) up to time t_1 : $\hat{\rho}'(t_1) = \mathcal{G}(t_1) \hat{\rho}'(0)$.

- Response function evaluation: $R^{(1)}(t_1) = \text{itr}\{\hat{\mu}\hat{\rho}'(t_1)\}/\hbar$, and obtain $I(\omega)$ via FFT.

2. 2D correlation IR spectra

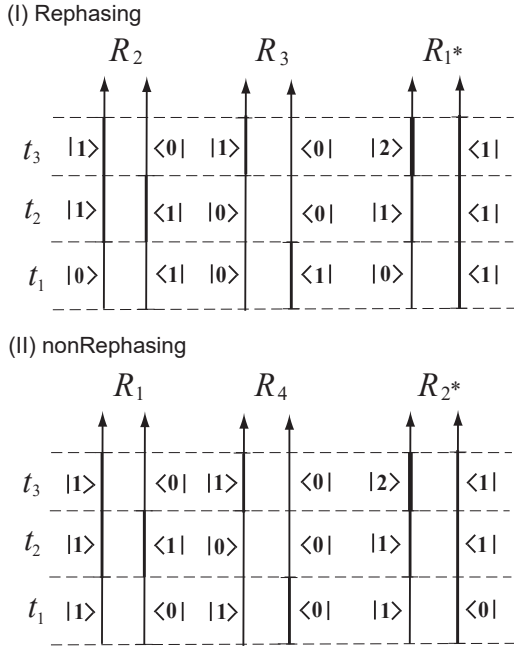


FIG. 1. Optical Liouville pathways in 2D vibrational spectroscopy for rephasing contribution. In each diagram, the left-hand line depicts the time evolution of the ket state $|\mathbf{n}\rangle$, while the right-hand line depicts that of the bra state $\langle\mathbf{n}'|$. The complex-conjugate pathways, obtained by interchanging the left and right states, are not shown.

For 2DIR experiments, three laser pulses with wavevectors \mathbf{k}_1 , \mathbf{k}_2 , and \mathbf{k}_3 are applied sequentially to the sample at times 0, t_1 , and $t_1 + t_2$. These pulses generate a four-wave mixing signal field at $t_1 + t_2 + t_3$ in the phase-matched directions.⁷ The signal is described by the third-order nonlinear response function^{44,45}

$$R^{(3)}(t_3, t_2, t_1) = \left(\frac{i}{\hbar}\right)^3 \text{tr}\{\hat{\mu}\mathcal{G}(t_3)\hat{\mu}^\times\mathcal{G}(t_2)\hat{\mu}^\times\mathcal{G}(t_1)\hat{\mu}^\times\hat{\rho}^{\text{eq}}\}. \quad (25)$$

Since $R^{(3)}(t_3, t_2, t_1)$ contains three $\hat{\mu}^\times$, the expression consists of eight terms.

Among them, the rephasing (echo) signal generated along the $\mathbf{k}_1 = \mathbf{k}_3 - \mathbf{k}_2$ phase-matched direction and the nonrephasing (virtual echo) signal detected along the

$\mathbf{k}_{\text{II}} = \mathbf{k}_3 - \mathbf{k}_2 + \mathbf{k}_1$ direction are evaluated from^{8–10,53–58}

$$R_{\text{I}}^{(3)}(t_3, t_2, t_1) = \left(\frac{i}{\hbar}\right)^3 \text{tr}\{\hat{\mu}\mathcal{G}(t_3)\hat{\mu}^\times\mathcal{G}(t_2)\hat{\mu}^\times\mathcal{G}(t_1)\hat{\mu}^\times\hat{\rho}^{\text{eq}}\}, \quad (26)$$

and

$$R_{\text{II}}^{(3)}(t_3, t_2, t_1) = \left(\frac{i}{\hbar}\right)^3 \text{tr}\{\hat{\mu}\mathcal{G}(t_3)\hat{\mu}^\times\mathcal{G}(t_2)\hat{\mu}^\times\mathcal{G}(t_1)\hat{\mu}^\times\hat{\rho}^{\text{eq}}\}, \quad (27)$$

respectively, where $\hat{\mu}_\rightarrow\hat{A} \equiv \hat{A}\hat{\mu}$ and $\hat{\mu}_\leftarrow\hat{A} \equiv \hat{\mu}\hat{A}$ for any operator \hat{A} .

By performing the double Fourier transform of Eqs. (26) and (27) with respect to t_1 and t_3 , we obtain the 2D rephasing spectrum

$$S_{\text{R}}(\Omega_3, \Omega_1; t_2) = \text{Im} \int \int_0^\infty dt_3 dt_1 e^{i\Omega_3 t_3 + i\Omega_1 t_1} R_{\text{I}}^{(3)}(t_3, t_2, t_1), \quad (28)$$

and 2D nonrephasing spectrum

$$S_{\text{NR}}(\Omega_3, \Omega_1; t_2) = \text{Im} \int \int_0^\infty dt_3 dt_1 e^{i\Omega_3 t_3 + i\Omega_1 t_1} R_{\text{II}}^{(3)}(t_3, t_2, t_1), \quad (29)$$

respectively.

The individual 2D rephasing and nonrephasing spectra exhibit distorted line shapes (phase-twisted lines), because the double Fourier transform mixes absorptive and dispersive features. By adding the rephasing and nonrephasing spectra with equal weights, the dispersive contributions cancel, yielding the 2D correlation spectrum with purely absorptive line shapes:^{9,10}

$$S_{\text{C}}(\Omega_3, \Omega_1; t_2) \equiv S_{\text{R}}(\Omega_3, -\Omega_1; t_2) + S_{\text{NR}}(\Omega_3, \Omega_1; t_2). \quad (30)$$

The procedure for calculating the 2D correlation spectrum using Eqs. (21)–(23) is summarized below, taking the rephasing contribution R_2 in Fig. 1(I) as an illustrative example.

- Initial condition: The method for setting the initial conditions $\hat{\rho}_{\{\mathbf{n}_s\}}^{\text{eq}} = |\mathbf{0}\rangle\langle\mathbf{0}|$ is the same as for linear absorption.
- First interaction ($t = 0$): $\hat{\rho}'(0) = \hat{\rho}^{\text{eq}}\hat{\mu}$, yielding $|\mathbf{0}\rangle\langle\mathbf{1}|$. Propagation under HEOM up to t_1 : $\hat{\rho}'(t_1) = \mathcal{G}(t_1)\hat{\rho}'(0)$.
- Second interaction (t_1): $\hat{\rho}''(t_1) = \hat{\mu}\hat{\rho}'(t_1)$. Propagation up to $t_1 + t_2$: $\hat{\rho}''(t_1 + t_2) = \mathcal{G}(t_2)\hat{\rho}''(t_1)$.
- Third interaction ($t_1 + t_2$): $\hat{\rho}'''(t_1 + t_2) = \hat{\mu}\hat{\rho}''(t_1 + t_2)$. Propagation up to $t_1 + t_2 + t_3$: $\hat{\rho}'''(t_1 + t_2 + t_3) = \mathcal{G}(t_3)\hat{\rho}'''(t_1 + t_2)$.

- Response function evaluation: $R_2(t_1, t_2, t_3) = \langle \mathbf{0} | \hat{\mu} \hat{\rho}'''(t_1 + t_2 + t_3) | \mathbf{0} \rangle$ and $\langle \mathbf{2} | \hat{\mu} \hat{\rho}'''(t_1 + t_2 + t_3) | \mathbf{2} \rangle$.

The contributions from the other diagrams can also be calculated in the same manner. Contributions containing only population states are referred to as rephasing part at t_2 intervals, whereas contributions involving other coherences are termed non-rephasing part.

III. COMPUTATIONAL FRAMEWORK FOR HEOM-2DVS

Numerical integration of the HEOM has enabled detailed analyses of diverse open quantum dynamical problems. Consequently, many practical implementations have been developed.^{69–79} The HEOM-2DVS used in this study differs from conventional formulations in that it explicitly incorporates counter terms derived from the MAB model and treats three independent thermal baths with coupled LL+SL interactions. Because intramolecular vibrational excitation energies exceed thermal energies, a larger low-temperature correction term is required. Furthermore, evaluating the 2D correlation spectrum requires scanning t_1 and t_3 for each value of t_2 and performing Fourier transforms, resulting in substantial computational cost. Thus, reducing numerical expense is essential when applying HEOM to the MAB. Although the overall code structure is simple, we adopt the Padé approximation, to represent the fluctuation and dissipation operators.⁶⁸ The HEOM expressed in terms of the Padé-approximated frequencies ν_k^α ($k = 0, 1, \dots, K_\alpha$; $\nu_0^\alpha = \gamma_\alpha$) follow the forms given in Refs. 80 and 81.

The model used in this simulation is the same as that adopted in our earlier classical calculations.⁴⁹ Calculations based on the Wigner distribution function are well suited for studying intermolecular vibrations whose excitation energies are close to the thermal energy,⁵⁰ whereas solving the HEOM in the energy-eigenstate representation is numerically more efficient for quantum treatments of intramolecular vibrations with much higher excitation energies. Thus, the HEOM for MAB and the corresponding QHFEP provide complementary capabilities. Accordingly, the input for the HEOM used in this code was standardized to match the format of the HFPE. Specifically, the inputs consist of the parameter values appearing in Eqs.(1)–(7).

Time evolution of the HEOM was performed using the Runge–Kutta method. The implementation efficiently manages large queues through external libraries. Further details are provided in the accompanying `README.txt` file.

Numerical calculations were performed on a PC: (i) Intel(R) Core(TM) i9-9900K 8-core, RAM: 32GB. The OS we used was almalinux8, the compiler was gcc 14, and we used Python 3.12. The libraries used in C++ are Eigen, hdf5-1.14.6. The libraries used in Python are numpy, matplotlib, h5py, and pybind11.

IV. NUMERICAL RESULTS

As a demonstration of the HEOM-2DVS framework, we computed the linear absorption (1DIR) spectra and the 2D correlated IR spectra of the intramolecular vibrational modes of liquid water using both (i) two-mode and (ii) three-mode models. Within this framework, the number of energy eigenstates used to represent each vibrational mode can be varied. Quantitatively reliable calculations generally require four or more states per mode⁴⁶. In the present work, however, we examine the extent to which three eigenstates per mode—the minimal basis necessary for 2DVS simulations—can capture the essential features of the dynamics. Although the current implementation of HEOM-2DVS does not employ GPU acceleration, it is capable of generating 2D correlation IR spectra within approximately seven hours on an Intel i9-9900K processor.

For (i) the two-mode calculations, the fundamental frequencies were set to (1) stretch mode ($\omega_1 = 3520 \text{ cm}^{-1}$) and (2) bend mode ($\omega_2 = 1710 \text{ cm}^{-1}$) to enable direct comparison with the DHEOM-MLWS results obtained in the Wigner-space representation.⁵² The parameters adopted here were chosen to match those used in that calculation and are summarized in Table I.

For (ii) the three-mode calculations, the fundamental frequencies were set to (1) asymmetric stretch ($\omega_1 = 3570 \text{ cm}^{-1}$), (1') symmetric stretch ($\omega_{1'} = 3470 \text{ cm}^{-1}$), and (2) bending ($\omega_2 = 1710 \text{ cm}^{-1}$) and employ the parameter values for the strong intermolecular-coupling case in classical simulations based on the CHFPE-2DVS framework.⁴⁹ The parameter are summarized in Tables II and III.

We note that the stretching and anti-stretching modes are not distinguishable in the 2DIR spectrum. Consequently, in the three-mode case, their individual parameters and mutual coupling cannot be uniquely determined from the 2D spectral data alone.⁴⁸ Thus, the intermode-couplings presented in Table III is treated not as a fixed parameter but as an adjustable variable used to fit the MD simulation results and experimental results.

A. Linear Absorption (1D) spectra

The 1DIR spectra for the quantum two-mode case (Table I) and for the classical and quantum three-mode cases (Tables II and III) are shown in Fig. 2. The quantum two-mode and three-mode spectra were computed using HEOM-2DVS, whereas the classical three-mode spectrum was obtained using CHFPE-2DVS.⁴⁹

In IR spectra, the stretching and bending peaks of high-frequency intramolecular modes appear blue-shifted in classical descriptions due to quantum anharmonic effects.⁴⁶ Although the present MAB model was constructed from classical 2D IR–Raman simulations, the underlying force field (POLI2VS)⁸³ was originally developed for quantum MD. Consequently, even though the

TABLE I. Parameter values for (i) the two-mode MAB model consisting of the (1) stretching mode and (2) bending mode. The values were taken from Refs. 51 and 52. The fundamental frequency was set to $\omega_0 = 4000 \text{ cm}^{-1}$. The anharmonic mode-mode coupling and dipole elements are $\tilde{g}_{121'} = 0$, $\tilde{g}_{11'2} = 0.2$, and $\tilde{\mu}_{11'} = 2.0 \times 10^{-3}$. The normalization parameters are defined as $\tilde{\zeta}_s \equiv (\omega_0/\omega_s)^2 \zeta_s$, $\tilde{V}_{LL}^{(s)} \equiv (\nu_s/\nu_0) V_{LL}^{(s)}$, $\tilde{V}_{SL}^{(s)} \equiv V_{SL}^{(s)}$, $\tilde{g}_{s3} \equiv (\nu_s/\nu_0)^3 g_{s3}$, $\tilde{\mu}_s \equiv (\mu_0/\omega_s) \mu_s$, and $\tilde{\mu}_{ss} \equiv (\nu_0/\omega_s)^2 \mu_{ss}$.

s	$\nu_s (\text{cm}^{-1})$	γ_s/ω_0	$\tilde{\zeta}_s$	$\tilde{V}_{LL}^{(s)}$	$\tilde{V}_{SL}^{(s)}$	\tilde{g}_{s3}	$\tilde{\mu}_s$	$\tilde{\mu}_{ss}$
1	3520	5.0×10^{-3}	9	0	1.0	-5.0×10^{-1}	3.3	1.2×10^{-2}
2	1710	2×10^{-2}	0.8	0	1.0	-7×10^{-1}	1.8	0

TABLE II. Parameter values of (ii) the three-mode MAB model for the (1) asymmetric stretching, (1') symmetric stretching, and (2) bending modes. To enable comparison with the classical results, the parameters were set to the same values as those used in the three-mode CHFPE calculation in Ref. 49. The fundamental frequency was fixed at $\omega_0 = 4000 \text{ cm}^{-1}$. The intermode coupling strengths and optical properties are given in Table III.

s	$\nu_s (\text{cm}^{-1})$	γ_s/ω_0	$\tilde{\zeta}_s$	$\tilde{V}_{LL}^{(s)}$	$\tilde{V}_{SL}^{(s)}$	\tilde{g}_{s3}	$\tilde{\mu}_s$	$\tilde{\mu}_{ss}$
1	3570	5.0×10^{-3}	9	0	1.0	-5.0×10^{-1}	3.3	1.2×10^{-2}
1'	3470	5.0×10^{-3}	9	0	1.0	-5.0×10^{-1}	3.3	1.2×10^{-2}
2	1710	2×10^{-2}	0.8	0	1.0	-7×10^{-1}	1.8	0

TABLE III. Parameter values of the anharmonic intermode couplings and optical properties for (ii) the three-mode MAB model (see also Table II). The intermolecular coupling strength employed here corresponds to the strong-coupling case in Ref. 49.

$s - s'$	$\tilde{g}_{ss'}$	$\tilde{g}_{s^2 s'}$	$\tilde{g}_{ss'^2}$	$\tilde{\mu}_{ss'}$
$1 - 1'$	-5×10^{-3}	0.32	-4.2×10^{-3}	0
$1 - 2$	1×10^{-7}	$-2,6 \times 10^{-2}$	4×10^{-4}	2.0×10^{-3}
$1' - 2$	-8×10^{-4}	1.2×10^{-1}	-1.2×10^{-2}	2.0×10^{-3}

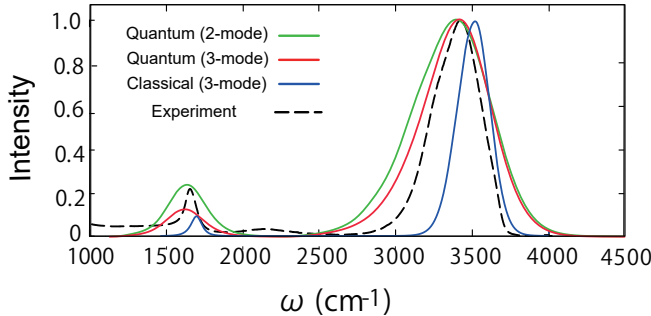


FIG. 2. Linear absorption (1DIR) spectrum of water calculated for the two-mode and three-mode MAB models using HEOM-2DVS (quantum) and CHFPE-2DVS (classical). The experimental IR data⁸² are shown as dashed black curves for comparison. Each spectrum is normalized to its maximum peak intensity. The blue solid curves represent the three-mode classical result, while the green and red solid curves represent the two-mode and three-mode quantum results, respectively.

MAB model is derived from classical MD trajectories, it yields vibrational spectra that remain accurate when

combined with quantum HEOM calculations, producing results comparable to quantum MD simulations using POLI2VS.⁸⁴ This suggests that a quantum MAB model can, in principle, be extracted from 2D spectra generated by first-principles classical MD simulations in which nuclear motion is treated classically.^{51,52} In addition to the blue-shifted peak positions, the classical spectra exhibit narrower linewidths than the experimental spectra, reflecting the inability of classical dynamics to capture broadening associated with zero-point fluctuations.

Both the two-mode and three-mode quantum calculations successfully reproduce the experimental peak positions, but the corresponding linewidths are overestimated relative to experimental results. This overestimation is likely attributable to the limited number of energy eigenstates included in the calculations. Although high-energy states should not contribute significantly in the absence of a thermal bath, energy states that interact strongly with a bath possessing a continuous energy distribution can mix with lower levels and influence the dynamics. In particular, the bending mode, which has very low thermal excitation energy, exhibits substantial linewidth broadening, indicating that additional eigenstates are required for an accurate description.

Despite these limitations, the three-level energy-eigenstate description remains an efficient framework for exploring quantum effects involving three intramolecular

modes at relatively low computational cost. It also serves as a valuable complement to DHEOM-MLWS, which is restricted to two-mode systems.

B. 2D Correlation IR Spectra

We now present the 2D correlation IR spectra for the two-mode and three-mode cases. The 2D results for the classical description are shown in Ref. 49.

1. 2 Modes (one stretch-bend) case

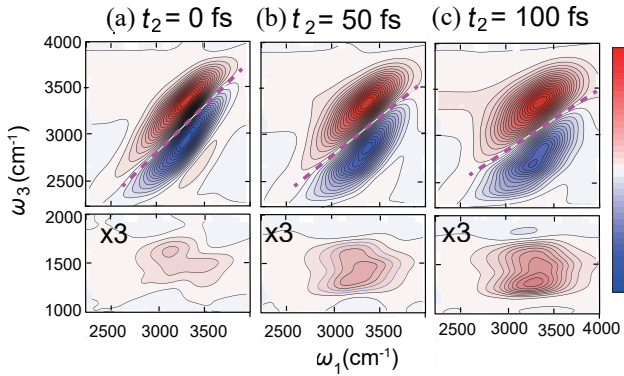


FIG. 3. 2D correlation IR spectra for the stretching and stretching→bending motions calculated using the two-mode model, which includes (1) the OH stretching mode ($\omega_1 = 3520 \text{ cm}^{-1}$), and (2) the HOH bending mode ($\omega_2 = 1710 \text{ cm}^{-1}$). Spectral intensities were normalized to the maximum amplitude of stretching mode. Because the peak intensity of the lower panels is weaker than in the upper panel, the contour interval was tripled for clarity.

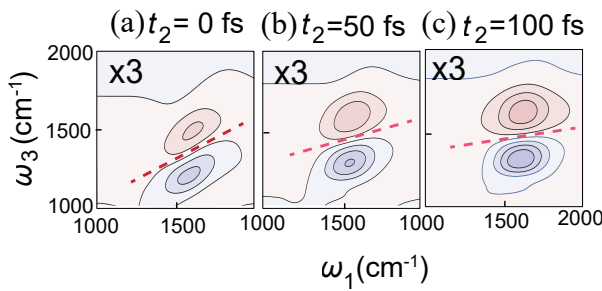


FIG. 4. 2D correlation IR spectra for the bending motion for the two-mode case. As the peak intensity was weaker than that in the upper panel of Fig. 3, the contour interval was tripled for emphasis.

We first present the results for the two-mode case and

discuss the differences in the description that appear in the DHEOM-MLWS results.⁵²

Figures 3 and 4 illustrate 2D correlation IR spectra calculated for the stretching–bending (1–2) modes. Each peak near $(\omega_1, \omega_3) = (3400 \text{ cm}^{-1}, 3400 \text{ cm}^{-1})$ in the upper panel corresponds to the stretching mode. The red positive peaks and blue negative peaks arise from the $|0\rangle_s \rightarrow_s |1\rangle_s \rightarrow |0\rangle_s$ and $|0\rangle_s \rightarrow_s |1\rangle_s \rightarrow |2\rangle_s$ pathways for $s = 1$, respectively, where $|n\rangle_s$ denotes the n th vibrational eigenstate of mode s .

The orientation of the red dashed nodal lines reflects the degree of noise correlation (non-Markovian effects) between the vibrational coherences during t_1 and t_3 . A direction parallel to the ω_1 axis corresponds to the uncorrelated limit, whereas alignment along the $\omega_1 = \omega_3$ diagonal corresponds to the fully correlated limit.^{55–57} The peak width parallel to the $\omega_1 = \omega_3$ line reflects inhomogeneous broadening, while the width perpendicular to this line reflects homogeneous broadening.^{20,85}

The lower panel of Fig. 3 display the cross peaks associated with the stretching→bending transition (e.g., $|0\rangle_1|0\rangle_2 \rightarrow |1\rangle_1|0\rangle_2 \sim |0\rangle_1|1\rangle_2 \rightarrow |0\rangle_1|0\rangle_2$).²⁰ The coupling peak observed at $t_2 = 0$ arises from coherent energy exchange between the two modes. While this coherent peak decays rapidly, the peak appearing around $t_2 = 50$ fs reflects population transfer, and its intensity increases with increasing t_2 .⁵²

2D correlation IR spectra for the bending mode is presented in Fig. 4. The DHEOM-MLWS results⁵² show that the nodal line is initially horizontal, whereas the HEOM-2DES results exhibit strong coherence, leading to a clear relaxation of the nodal line.

The results obtained from HEOM-2DVS are qualitatively similar to those of DHEOM-MLWS, except that the diagonal (inhomogeneous) broadening of the two peaks spans a wider range, extending from approximately 2600 to 3800 cm^{-1} rather than 3200–3700 cm^{-1} , whereas the off-diagonal (homogeneous) broadening is narrower.²⁰ As discussed in the 1D spectrum, this broadening is attributed to the strong quantum character of the enhanced zero-point vibrations. Because this broadening reflects coherence, the inhomogeneity manifested as off-diagonal broadening remains small.

2. 3 Modes (two stretch-bend) case

Figures 5 and 6 shows the 2D correlation spectra calculated for (1) the OH stretching mode with $\omega_1=3570 \text{ cm}^{-1}$, (1') OH anti-stretching mode with $\omega_1'=3470 \text{ cm}^{-1}$, and (2) HOH bending mode with $\omega_2=1710 \text{ cm}^{-1}$.^{86–88}

The stretching→bending cross peaks (Fig. 6) are much weaker than in the two-mode case as we observed in 1DIR spectra. Their profiles are elongated only along ω_1 , reflecting identical anharmonicities of the two stretching modes. The peak intensities increase with t_2 because of population transfer.

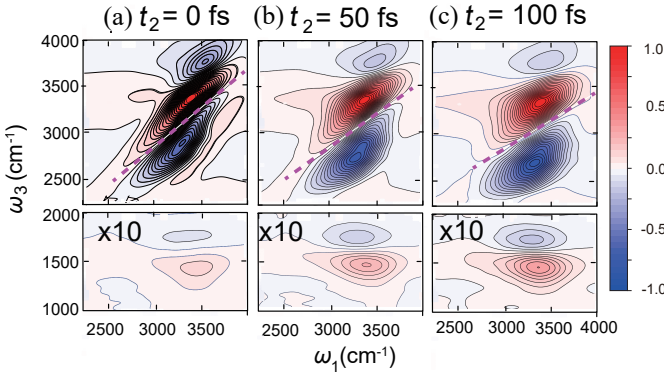


FIG. 5. 2D correlation IR spectra for the stretching and stretching→bending motions calculated using the three-mode model, which includes (1) the OH stretching mode ($\omega_1 = 3570 \text{ cm}^{-1}$), (1') the OH anti-stretching mode ($\omega_{1'} = 3470 \text{ cm}^{-1}$), and (2) the HOH bending mode ($\omega_2 = 1710 \text{ cm}^{-1}$). The mode-mode coupling among the three modes was set to the strong-coupling values listed in Table III. Spectral intensities were normalized to the maximum amplitude of stretch peak. Because the peak intensity of the lower panels is weaker than in the upper panel, the contour interval was increased by a factor of ten for emphasis.

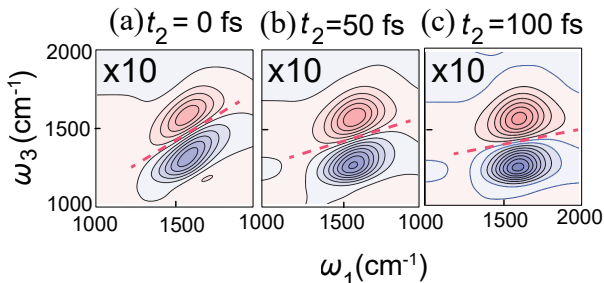


FIG. 6. Results for the same calculations as in Fig. 5, but for the bending modes of the three-mode model. Because the peak intensity is weaker than in the upper panel of Fig. 5, the contour interval was increased by a factor of ten for clarity.

The major difference from the two-mode results is the appearance of a third blue peak on the high-frequency side, located above the red peak. This feature can be interpreted as arising from the splitting of the two stretching-mode peaks into lower- and higher-frequency components due to large intermodal coupling, leading to the formation of the $|1^\pm\rangle$ levels.

As in the two-mode case, the large red and blue peaks can be assigned to the $|0\rangle \rightarrow |1^\pm\rangle \rightarrow |0\rangle$ and $|0\rangle \rightarrow |1^-\rangle \rightarrow |2^-\rangle$ pathways, respectively, whereas the third blue peak originates from the $|0\rangle \rightarrow |1^\pm\rangle \rightarrow |2^+\rangle$ transition. These transitions proceed through coherent dynamics, with the associated peaks appearing immedi-

ately at $t_2 = 0$ and decaying as t_2 increases.

Although this third peak is not observed experimentally, it is attributed to the strong intermode coupling introduced in Ref. 49, which we adopted as an adjustable parameter in the present model.

V. CONCLUSION

In this work, we addressed the long-standing challenge of simulating 2D vibrational spectra in solution, particularly for intramolecular modes whose molecular vibrations are quantum-mechanically entangled with their environment.

To date, no simulation has successfully reproduced the 2D spectra of the intramolecular vibrations of water while combining MD with a quantitatively accurate description of quantum dissipation. Within these limitations, the MAB model provides a highly descriptive framework capable of reproducing experimental features while incorporating complex intermolecular interactions and the nonlinear system-bath couplings responsible for vibrational dephasing. By analyzing 2D signals within this model-based approach, one can clarify the physical origins of spectral line-shape features and obtain conceptual insights that are difficult to extract from fully detailed MD simulations.

The present code enables fast computation of 2D signals by representing each intramolecular vibration as a three-level system, although its descriptive power is lower than that of DHEOM-MLWS.^{51,52} For semiclassical intermolecular modes, the CHFPE-2DVS code for the three-mode MAB model remains superior in both accuracy and computational cost. Thus, the present code is complementary to existing approaches.

Our group is currently developing a machine learning (ML)-assisted algorithm that constructs MAB models suitable for HEOM calculations directly from MD trajectories, without relying on spectral fitting.^{42,43} The program developed in this study is also intended to be applied to models constructed in this manner.

In this paper, we limited ourselves to demonstration calculations without pursuing a detailed analysis. In a subsequent study, we will apply HEOM parameters constructed from MD trajectories using machine-learning techniques to analyze the 2D spectra of H₂O, D₂O, and HOD, and we will discuss the distinct underlying physical processes revealed through their IR spectra.⁸⁹

SUPPLEMENTARY MATERIAL

Numerical integration codes on the basis of HEOM formalism for 1D IR and 2D correlation IR are provided as supplemental materials. The manual can be found in the ReadMe.pdf file.

ACKNOWLEDGMENTS

Y. T. was supported by JST (Grant No. CREST 1002405000170).

AUTHOR DECLARATIONS

Conflict of Interest

The authors have no conflicts to disclose.

DATA AVAILABILITY

The data that support the findings of this study are available from the corresponding author upon reasonable request.

- ¹A. K. Covington and T. Dickinson, *Physical Chemistry of Organic Solvent Systems* (Springer, 1978).
- ²M. F. J. Mabesoone et al., “Solute–solvent interactions in modern physical organic chemistry,” *Journal of the American Chemical Society* **144**, 7565–7581 (2022).
- ³I. Ohmine and H. Tanaka, “Fluctuation, relaxations, and hydration in liquid water. hydrogen-bond rearrangement dynamics,” *Chemical Reviews* **93**, 2545–2566 (1993), <https://doi.org/10.1021/cr00023a011>.
- ⁴I. Ohmine and S. Saito, “Water dynamics : fluctuation, relaxation, and chemical reactions in hydrogen bond network rearrangement,” *Accounts of Chemical Research* **32**, 741–749 (1999).
- ⁵E. T. J. Nibbering and T. Elsaesser, “Ultrafast vibrational dynamics of hydrogen bonds in the condensed phase.” *Chemical reviews* **104** 4, 1887–1914 (2004).
- ⁶B. Bagchi, “Water in biological and chemical processes: From structure and dynamics to function,” *Cambridge Molecular Science* (2013), 10.1017/CBO9781139583947.
- ⁷S. Mukamel, *Principles of nonlinear optical spectroscopy*, 6 (Oxford University Press on Demand, 1999).
- ⁸P. Hamm, M. Lim, and R. M. Hochstrasser, “Non-markovian dynamics of the vibrations of ions in water from femtosecond infrared three-pulse photon echoes,” *Phys. Rev. Lett.* **81**, 5326–5329 (1998).
- ⁹N. Demirdöven, M. Khalil, and A. Tokmakoff, “Correlated vibrational dynamics revealed by two-dimensional infrared spectroscopy,” *Phys. Rev. Lett.* **89**, 237401 (2002).
- ¹⁰N. Demirdöven, M. Khalil, and A. Tokmakoff, “Correlated vibrational dynamics revealed by two-dimensional infrared spectroscopy,” *Phys. Rev. Lett.* **89**, 237401 (2002).
- ¹¹M. Cho, *Two-Dimensional Optical Spectroscopy* (CRC Press, 2009).
- ¹²P. Hamm and M. T. Zanni, *Concepts and Methods of 2D Infrared Spectroscopy* (Cambridge University Press, 2011).
- ¹³P. Hamm and A. Shalit, “Perspective: Echoes in 2d-Raman-THz spectroscopy,” *The Journal of Chemical Physics* **146**, 130901 (2017), <https://doi.org/10.1063/1.4979288>.
- ¹⁴J. B. Asbury, T. Steinel, K. Kwak, S. A. Corcelli, C. P. Lawrence, J. L. Skinner, and M. D. Fayer, “Dynamics of water probed with vibrational echo correlation spectroscopy,” *The Journal of Chemical Physics* **121**, 12431–12446 (2004).
- ¹⁵M. Cowan, B. Bruner, N. Huse, J. Dwyer, B. Chugh, E. Nibbering, T. Elsaesser, and R. Miller, “Ultrafast memory loss and energy redistribution in the hydrogen bond network of liquid H₂O,” *NATURE* **434**, 199–202 (2005).
- ¹⁶K. Ramasesha, L. De Marco, A. Mandal, and A. Tokmakoff, “Water vibrations have strongly mixed intra- and intermolecular character,” *Nature Chemistry* **5**, 935–940 (2013).
- ¹⁷P. Hamm and J. Savolainen, “Two-dimensional-Raman-Terahertz spectroscopy of water: Theory,” *The Journal of Chemical Physics* **136**, 094516 (2012), <https://doi.org/10.1063/1.3691601>.
- ¹⁸G. Mead, H.-W. Lin, I.-B. Magdău, T. F. I. Miller, and G. A. Blake, “Sum-frequency signals in 2d-terahertz-terahertz-raman spectroscopy,” *The Journal of Physical Chemistry B* **124**, 8904–8908 (2020), pMID: 32897705, <https://doi.org/10.1021/acs.jpcb.0c07935>.
- ¹⁹T. Begušić and G. A. Blake, “Two-dimensional infrared-raman spectroscopy as a probe of water’s tetrahedrality,” *Nature Communications* **14**, 1950 (2023).
- ²⁰Y. Tanimura and A. Ishizaki, “Modeling, calculating, and analyzing multidimensional vibrational spectroscopies,” *Accounts of Chemical Research* **42**, 1270–1279 (2009).
- ²¹S. Saito and I. Ohmine, “Fifth-order two-dimensional Raman spectroscopy of liquid water, crystalline ice Ih and amorphous ices: Sensitivity to anharmonic dynamics and local hydrogen bond network structure,” *The Journal of Chemical Physics* **125**, 084506 (2006), <https://doi.org/10.1063/1.2232254>.
- ²²T. Hasegawa and Y. Tanimura, “Calculating fifth-order Raman signals for various molecular liquids by equilibrium and nonequilibrium hybrid molecular dynamics simulation algorithms,” *The Journal of Chemical Physics* **125**, 074512 (2006).
- ²³Y. L. Li, L. Huang, R. J. Dwayne Miller, T. Hasegawa, and Y. Tanimura, “Two-dimensional fifth-order Raman spectroscopy of liquid formamide: Experiment and theory,” *The Journal of Chemical Physics* **128**, 234507 (2008).
- ²⁴T. Hasegawa and Y. Tanimura, “Nonequilibrium molecular dynamics simulations with a backward-forward trajectories sampling for multidimensional infrared spectroscopy of molecular vibrational modes,” *The Journal of Chemical Physics* **128**, 064511 (2008).
- ²⁵T. Yagasaki and S. Saito, “Ultrafast intermolecular dynamics of liquid water: A theoretical study on two-dimensional infrared spectroscopy,” *The Journal of Chemical Physics* **128**, 154521 (2008), <https://doi.org/10.1063/1.2903470>.
- ²⁶S. Saito and I. Ohmine, “Translational and orientational dynamics of a water cluster (H₂O)₁₀₈ and liquid water: Analysis of neutron scattering and depolarized light scattering,” *The Journal of Chemical Physics* **102**, 3566–3579 (1995), https://pubs.aip.org/aip/jcp/article-pdf/102/9/3566/19057921/3566_1_online.pdf.
- ²⁷S. Saito and I. Ohmine, “Third order nonlinear response of liquid water,” *The Journal of Chemical Physics* **106**, 4889–4893 (1997), https://pubs.aip.org/aip/jcp/article-pdf/106/12/4889/19096671/4889_1_online.pdf.
- ²⁸T. Yagasaki and S. Saito, “A novel method for analyzing energy relaxation in condensed phases using nonequilibrium molecular dynamics simulations: Application to the energy relaxation of intermolecular motions in liquid water,” *The Journal of Chemical Physics* **134**, 184503 (2011), <https://doi.org/10.1063/1.3587105>.
- ²⁹T. Yagasaki and S. Saito, “Fluctuations and relaxation dynamics of liquid water revealed by linear and nonlinear spectroscopy,” *Annual Review of Physical Chemistry* **64**, 55–75 (2013), <https://doi.org/10.1146/annurev-physchem-040412-110130>.
- ³⁰Z. Pan, T. Wu, T. Jin, Y. Liu, Y. Nagata, R. Zhang, and W. Zhuang, “Low frequency 2d raman-thz spectroscopy of ionic solution: A simulation study,” *The Journal of Chemical Physics* **142**, 212419 (2015), https://pubs.aip.org/aip/jcp/article-pdf/doi/10.1063/1.4917260/13242549/212419_1_online.pdf.
- ³¹H. Ito, T. Hasegawa, and Y. Tanimura, “Calculating two-dimensional THz-Raman-THz and Raman-THz-THz signals for various molecular liquids: The samplers,” *The Journal of Chemical Physics* **141**, 124503 (2014).
- ³²J.-Y. Jo, H. Ito, and Y. Tanimura, “Full molecular dynamics simulations of liquid water and carbon tetrachloride for

two-dimensional Raman spectroscopy in the frequency domain," *Chemical Physics* **481**, 245–249 (2016).

³³H. Ito, T. Hasegawa, and Y. Tanimura, "Effects of intermolecular charge transfer in liquid water on Raman spectra," *The Journal of Physical Chemistry Letters* **7**, 4147–4151 (2016).

³⁴S. Imoto, S. S. Xantheas, and S. Saito, "Ultrafast dynamics of liquid water: Frequency fluctuations of the OH stretch and the HOH bend," *The Journal of Chemical Physics* **139**, 044503 (2013), <https://doi.org/10.1063/1.4813071>.

³⁵S. Imoto, S. S. Xantheas, and S. Saito, "Ultrafast dynamics of liquid water: Energy relaxation and transfer processes of the OH stretch and the HOH bend," *The Journal of Physical Chemistry B* **119**, 11068–11078 (2015), PMID: 26042611, <https://doi.org/10.1021/acs.jpcb.5b02589>.

³⁶V. Babin, C. Leforestier, and F. Paesani, "Development of a "first-principles" water potential with flexible monomers: Dimer potential energy surface, vrt spectrum, and second virial coefficient," *Journal of Chemical Theory and Computation* **9**, 5395–5403 (2013).

³⁷V. Babin, G. R. Medders, and F. Paesani, "Development of a "first-principles" water potential with flexible monomers. ii. trimer potential energy surface, third virial coefficient, and small clusters," *Journal of Chemical Theory and Computation* **10**, 1599–1607 (2014).

³⁸G. R. Medders, V. Babin, and F. Paesani, "Development of a "first-principles" water potential with flexible monomers. iii. liquid phase properties," *Journal of Chemical Theory and Computation* **10**, 2906–2910 (2014).

³⁹A. Piryatinski, C. P. Lawrence, and J. L. Skinner, "Vibrational spectroscopy of HOD in liquid D₂O. v. infrared three-pulse photon echoes," *The Journal of Chemical Physics* **118**, 9672–9679 (2003), <https://doi.org/10.1063/1.1569474>.

⁴⁰A. Paarmann, T. Hayashi, S. Mukamel, and R. J. D. Miller, "Nonlinear response of vibrational excitons: Simulating the two-dimensional infrared spectrum of liquid water," *The Journal of Chemical Physics* **130**, 204110 (2009), <https://doi.org/10.1063/1.3139003>.

⁴¹S. Ueno and Y. Tanimura, "Modeling intermolecular and intramolecular modes of liquid water using multiple heat baths: Machine learning approach," *Journal of Chemical Theory and Computation* **16**, 2099–2108 (2020).

⁴²K. Park, J.-Y. Jo, and Y. Tanimura, "System–bath modeling in vibrational spectroscopy via molecular dynamics: A machine learning framework for hierarchical equations of motion (heom)," *The Journal of Chemical Physics* **163**, 214104 (2025).

⁴³K. Park, S. Ueno, and Y. Tanimura, "sbml4md: A computational platform for system–bath modeling via molecular dynamics powered by machine learning," *The Journal of Chemical Physics* **16x**, xxxx (2026).

⁴⁴Y. Tanimura, "Stochastic Liouville, Langevin, Fokker–Planck, and master equation approaches to quantum dissipative systems," *Journal of the Physical Society of Japan* **75**, 082001 (2006).

⁴⁵Y. Tanimura, "Numerically "exact" approach to open quantum dynamics: The hierarchical equations of motion (HEOM)," *The Journal of Chemical Physics* **153**, 020901 (2020).

⁴⁶A. Sakurai and Y. Tanimura, "Does \hbar play a role in multidimensional spectroscopy? reduced hierarchy equations of motion approach to molecular vibrations," *The Journal of Physical Chemistry A* **115**, 4009–4022 (2011).

⁴⁷T. Ikeda, H. Ito, and Y. Tanimura, "Analysis of 2D THz-Raman spectroscopy using a non-Markovian Brownian oscillator model with nonlinear system–bath interactions," *The Journal of Chemical Physics* **142**, 212421 (2015).

⁴⁸H. Ito and Y. Tanimura, "Simulating two-dimensional infrared-Raman and Raman spectroscopies for intermolecular and intramolecular modes of liquid water," *The Journal of Chemical Physics* **144**, 074201 (2016).

⁴⁹R. Hoshino and Y. Tanimura, "Analysis of intramolecular modes of liquid water in two-dimensional spectroscopy: A classical hierarchical equations of motion approach," *The Journal of Chemical Physics* **162**, 044105 (2025), https://pubs.aip.org/aip/jcp/article-pdf/doi/10.1063/5.0245564/20360227/044105_1_5.0245564.pdf.

⁵⁰R. Hoshino and Y. Tanimura, "A multimode classical hierarchical Fokker–Planck equations approach to molecular vibrations: Simulating two-dimensional spectra," *The Journal of Chemical Physics* **163**, 172501 (2025).

⁵¹H. Takahashi and Y. Tanimura, "Discretized hierachal equations of motion in mixed Liouville–Wigner space for two-dimensional vibrational spectroscopies of water," *The Journal of Chemical Physics* **158**, 044115 (2023), arXiv:2302.09799.

⁵²H. Takahashi and Y. Tanimura, "Simulating two-dimensional correlation spectroscopies with third-order infrared and fifth-order infrared–Raman processes of liquid water," *The Journal of Chemical Physics* **158**, 124108 (2023), arXiv:2302.09760.

⁵³A. Ishizaki and Y. Tanimura, "Modeling vibrational dephasing and energy relaxation of intramolecular anharmonic modes for multidimensional infrared spectroscopies," *The Journal of Chemical Physics* **125**, 084501 (2006).

⁵⁴A. Ishizaki and Y. Tanimura, "Dynamics of a multimode system coupled to multiple heat baths probed by two-dimensional infrared spectroscopy," *The Journal of Physical Chemistry A* **111**, 9269–9276 (2007).

⁵⁵J. D. Hybl, A. Albrecht Ferro, and D. M. Jonas, "Two-dimensional fourier transform electronic spectroscopy," *The Journal of Chemical Physics* **115**, 6606–6622 (2001), <https://doi.org/10.1063/1.1398579>.

⁵⁶N.-H. Ge, M. T. Zanni, and R. M. Hochstrasser, "Effects of vibrational frequency correlations on two-dimensional infrared spectra," *Journal of Physical Chemistry A* **106**, 962–972 (2002).

⁵⁷M. Khalil, N. Demirdöven, and A. Tokmakoff, "Obtaining absorptive line shapes in two-dimensional infrared vibrational correlation spectra," *Phys. Rev. Lett.* **90**, 047401 (2003).

⁵⁸Y. Tanimura, "Reduced hierarchy equations of motion approach with Drude plus Brownian spectral distribution: Probing electron transfer processes by means of two-dimensional correlation spectroscopy," *The Journal of Chemical Physics* **137**, 22A550 (2012).

⁵⁹A. Caldeira and A. Leggett, "Path integral approach to quantum brownian motion," *Physica A: Statistical Mechanics and its Applications* **121**, 587–616 (1983).

⁶⁰Y. Tanimura and P. G. Wolynes, "Quantum and classical Fokker–Planck equations for a Gaussian-Markovian noise bath," *Phys. Rev. A* **43**, 4131–4142 (1991).

⁶¹Y. Tanimura and S. Mukamel, "Two-dimensional femtosecond vibrational spectroscopy of liquids," *The Journal of Chemical Physics* **99**, 9496–9511 (1993).

⁶²Y. Tanimura, "Fifth-order two-dimensional vibrational spectroscopy of a Morse potential system in condensed phases," *Chemical Physics* **233**, 217–229 (1998).

⁶³K. Okumura and Y. Tanimura, "Two-time correlation functions of a harmonic system nonbilinearly coupled to a heat bath: Spontaneous Raman spectroscopy," *Phys. Rev. E* **56**, 2747–2750 (1997).

⁶⁴Y. Tanimura and T. Steffen, "Two-dimensional spectroscopy for harmonic vibrational modes with nonlinear system–bath interactions.ii. Gaussian-Markovian case," *Journal of the Physical Society of Japan* **69**, 4095–4106 (2000).

⁶⁵T. Kato and Y. Tanimura, "Two-dimensional Raman and infrared vibrational spectroscopy for a harmonic oscillator system nonlinearly coupled with a colored noise bath," *The Journal of Chemical Physics* **120**, 260–271 (2004).

⁶⁶Y. Tanimura and R. Kubo, "Time evolution of a quantum system in contact with a nearly Gaussian-Markoffian noise bath," *Journal of the Physical Society of Japan* **58**, 101–114 (1989).

⁶⁷R. Feynman and F. Vernon, "The theory of a general quantum system interacting with a linear dissipative system," *Annals of Physics* **24**, 118–173 (1963).

⁶⁸J. Hu, R.-X. Xu, and Y. Yan, “Communication: Padé spectrum decomposition of Fermi function and Bose function,” *The Journal of Chemical Physics* **133**, 101106 (2010).

⁶⁹Q. Shi and E. Geva, “A new approach to efficient hierarchical equations of motion for quantum dissipative systems,” *Journal of Chemical Physics* **131**, 034511 (2009).

⁷⁰Q. Shi, Y. Xu, Y. Yan, and M. Xu, “Efficient propagation of the hierarchical equations of motion using the matrix product state method,” *The Journal of Chemical Physics* **148**, 174102 (2018).

⁷¹T. Ikeda and G. D. Scholes, “Generalization of the hierarchical equations of motion theory for efficient calculations with arbitrary correlation functions,” *The Journal of Chemical Physics* **152**, 204101 (2020).

⁷²T. Ikeda and A. Nakayama, “Collective bath coordinate mapping of “hierarchy” in hierarchical equations of motion,” *The Journal of Chemical Physics* **156**, 104104 (2022).

⁷³Y.-T. Huang, P.-C. Kuo, N. Lambert, M. Cirio, S. Cross, S.-L. Yang, F. Nori, and Y.-N. Chen, “An efficient julia framework for hierarchical equations of motion in open quantum systems,” *Communications Physics* **6**, 313 (2023).

⁷⁴Y. Ke, “Tree tensor network state approach for solving hierarchical equations of motion,” *Journal of Chemical Physics* **158**, 211102 (2023).

⁷⁵R. Borrelli and S. Dolgov, “Expanding the range of hierarchical equations of motion by tensor-train implementation,” *The Journal of Physical Chemistry B* **125**, 5397–5407 (2021), pMID: 33980011.

⁷⁶H. Takahashi and R. Borrelli, “Tensor-train format hierarchical equations of motion formalism: Charge transfer in organic semiconductors via dissipative holstein models,” *Journal of Chemical Theory and Computation* **20**, 7052–7064 (2024), pMID: 39152908.

⁷⁷X. Chen and I. Franco, “Bexcitonics: Quasiparticle approach to open quantum dynamics,” *The Journal of Chemical Physics* **160**, 204116 (2024).

⁷⁸X. Chen and I. Franco, “Tree tensor network hierarchical equations of motion based on time-dependent variational principle for efficient open quantum dynamics in structured thermal environments,” *The Journal of Chemical Physics* **163**, 104109 (2025).

⁷⁹Z. Shi, H. Zhou, L. Huang, R. Xie, and L. Wang, “Hierarchical equations of motion solved with the multiconfigurational ehrenfest ansatz,” *The Journal of Chemical Physics* **163**, 224103 (2025).

⁸⁰Y. Iwamoto and Y. Tanimura, “Linear absorption spectrum of a quantum two-dimensional rotator calculated using a rotationally invariant system-bath hamiltonian,” *The Journal of Chemical Physics* **149**, 084110 (2018).

⁸¹Y. Iwamoto and Y. Tanimura, “Open quantum dynamics of a three-dimensional rotor calculated using a rotationally invariant system-bath Hamiltonian: Linear and two-dimensional rotational spectra,” *The Journal of Chemical Physics* **151**, 044105 (2019).

⁸²Y. Maréchal, “The molecular structure of liquid water delivered by absorption spectroscopy in the whole IR region completed with thermodynamics data,” *Journal of Molecular Structure* **1004**, 146–155 (2011).

⁸³T. Hasegawa and Y. Tanimura, “A polarizable water model for intramolecular and intermolecular vibrational spectroscopies,” *The Journal of Physical Chemistry B* **115**, 5545–5553 (2011).

⁸⁴X. Liu and J. Liu, “Critical role of quantum dynamical effects in the Raman spectroscopy of liquid water,” *Molecular Physics* **116**, 755–779 (2018), <https://doi.org/10.1080/00268976.2018.1434907>.

⁸⁵K. Lazonder, M. S. Pshenichnikov, and D. A. Wiersma, “Easy interpretation of optical two-dimensional correlation spectra,” *Opt. Lett.* **31**, 3354–3356 (2006).

⁸⁶L. De Marco, J. A. Fournier, M. Thämer, W. Carpenter, and A. Tokmakoff, “Anharmonic exciton dynamics and energy dissipation in liquid water from two-dimensional infrared spectroscopy,” *The Journal of Chemical Physics* **145**, 094501 (2016), <https://aip.scitation.org/doi/pdf/10.1063/1.4961752>.

⁸⁷W. B. Carpenter, J. A. Fournier, R. Biswas, G. A. Voth, and A. Tokmakoff, “Delocalization and stretch-bend mixing of the HOH bend in liquid water,” *The Journal of Chemical Physics* **147**, 084503 (2017), <https://doi.org/10.1063/1.4987153>.

⁸⁸N. H. C. Lewis, B. Dereka, Y. Zhang, E. J. Maginn, and A. Tokmakoff, “From networked to isolated: Observing water hydrogen bonds in concentrated electrolytes with two-dimensional infrared spectroscopy,” *The Journal of Physical Chemistry B* **126**, 5305–5319 (2022), pMID: 35829623, <https://doi.org/10.1021/acs.jpcb.2c03341>.

⁸⁹K. Park, R. Hoshino, and Y. Tanimura, “Isotope effects in 2d infrared spectra of water: HEOM analysis of molecular dynamics-based machine learning models,” *The Journal of Chemical Physics* **16x**, xxxx (2026).